Advanced Electronic Materials

www.advelectronicmat.de

Research Article OPEN ACCESS

Interactions Enhance Ramp Reversal Memory in Locally Phase Separated Materials

Y. Sun[1,2] | M. Alzate Banguero[3] | P. Salev[4] | Ivan K. Schuller[5] | L. Aigouy[3] | A. Zimmers[3] | E. W. Carlson[1,2]

[1]Department of Physics and Astronomy, Purdue University, West Lafayette, Indiana, USA | [2]Purdue Quantum Science and Engineering Institute, West Lafayette, Indiana, USA | [3]Laboratoire de Physique et d'Étude des Matériaux, ESPCI Paris, PSL Université, CNRS, Sorbonne Université, Paris, France | [4]Department of Physics and Astronomy, University of Denver, Denver, Colorado, USA | [5]Department of Physics and Center for Advanced Nanoscience, University of California-San Diego, La Jolla, California, USA

Correspondence: A. Zimmers (azimmers@espci.fr) | E. W. Carlson (ewcarlson@purdue.edu)

Received: 21 July 2025 | **Revised:** 12 November 2025 | **Accepted:** 14 November 2025

Keywords: defect motion | memory | memristor | metal–insulator transition | Mott transition | phase separation | random field Ising model

The ramp-reversal memory (RRM) effect in metal–insulator transition metal oxides (TMOs), a non-volatile resistance change induced by repeated temperature cycling, has attracted considerable interest in neuromorphic computing and non-volatile memory devices. Our previous defect motion model successfully explained RRM in vanadium dioxide (VO_2), capturing observed critical temperature shifts and memory accumulation throughout the sample. However, this approach lacked interactions between metallic and insulating domains. Here, we extend our model by combining a correlated Random Field Ising Model with defect diffusion-segregation, enabling accurate hysteresis modeling while predicting the relationship between RRM and domain interactions. Our simulations demonstrate that the maximum RRM occurs when the turnaround temperature approaches the inflection point. This peak in RRM vs. turnaround temperature is consistent with prior transport measurements, as well as our own optical measurements reported here. Significantly, we find that increasing nearest-neighbor interactions enhances the maximum memory effect, thus providing a clear mechanism for optimizing RRM performance. Since our model employs minimal assumptions, we predict that RRM should be a *widespread phenomenon* in materials exhibiting patterned phase coexistence of electronic domains. This work not only advances fundamental understanding of memory behavior in TMOs but also establishes a much-needed theoretical framework for optimizing device applications.

1 | Introduction

Neuromorphic computing has recently garnered significant attention as a promising avenue to address the growing energy demands of large language models and other complex artificial intelligence (AI) applications. Moreover, local thermal dissipation in conventional architectures may limit packing density and scaling for future AI applications [1]. By emulating the structure and function of biological brains, neuromorphic computing offers the potential for energy-efficient computation and a more native hardware platform for AI tasks.

One area of particular interest for developing neuromorphic devices is the study of the insulator–metal transition (IMT) in transition-metal oxides (TMOs), which uniquely exhibit volatile resistive switching between high- and low-resistance states in response to electrical [2] or thermal [3, 4] stimuli. These threshold-driven transitions enable the implementation of key neuromorphic components, including spiking neurons that fire when stimulated above a threshold [5] and active signal transmission lines similar to biological axons [6]. However, volatile switching alone is insufficient for brain-inspired computing, which requires persistent memory to enable synaptic learning

---

and adaptation. Thus, identifying a single material that can provide both neuron-like volatile switching and synaptic nonvolatile switching is essential for fully scalable neuromorphic chips [7–9].

Two complementary properties make vanadium dioxide (VO_2) a strong candidate. First, as in other TMOs, it exhibits a thermally induced Mott insulator–metal transition, generating a resistivity change of up to five orders of magnitude. However, this transition occurs near 68 °C [10, 11], just above room temperature, thereby enhancing its practicality for integration into neuron-like applications [12, 13]. Second, VO_2 exhibits phase separation during the IMT [14], a feature that can potentially be controlled and harnessed for nonvolatile memory. Current approaches to do so include ion bombardment [15], electrical-field breakdown [16], gating [17], and thermal coupling [18–20]. Although each approach represents a significant step forward, major roadblocks remain: ion bombardment is tunable but not rewritable and requires sophisticated material preparation; electrical-field breakdown is easily achievable but neither reconfigurable nor tunable due to uncontrolled stochastic filament formation; gating is slow and highly dependent on sample quality as it relies on electric-field-induced ion motion; and thermal coupling is hardly reconfigurable, being primarily determined by initial lithographic separation of oscillators (0.2 μm to 20 μm [18–20]). Harnessing VO_2's potential for nonvolatile synapse behavior thus requires a new approach, accompanied by a theoretical model for understanding and manipulating the phase-separated state, which is essential to establish the tunable, non-stochastic, and reprogrammable control needed for next-generation neuromorphic computing [21].

In 2017, by applying a "ramp reversal" temperature protocol, Vardi et al. reported a multi-level, reconfigurable, nonvolatile memory effect, revealed by a pronounced (∼20%) increase in resistivity [22]. This Ramp Reversal Memory (RRM) has since been reported by the same group in $NdNiO_3$, V_2O_3, and 1T-TaS_2 [22–24]. They attributed this memory formation to "scars"—structural defects analogous to silt deposits at a flood boundary—that raise the local transition temperature and form at phase boundaries during the IMT. Our earlier experimental observations measuring spatially resolved reflected optical intensity revealed that the RRM effect occurs throughout the entire sample rather than only at phase boundaries, and moreover that it involves both increases and decreases in the local transition temperature (T_c) [25]. These results prompted us to develop the defect motion model in which the RRM effect originates from the motion of point defects within VO_2, providing a framework to explain the spatially distributed accumulation of memory. In this model, the redistribution of defect density can either increase or decrease the local T_c throughout the bulk of the sample, in addition to producing scar-like structures at phase boundaries, suggesting that our approach may also capture key aspects of the scar model.

However, our previous model of RRM did not include interactions between metal and insulator regions, whereas multiple studies have indicated the need for interactions in order to capture the physics of the phase separated regime. For example, the presence of avalanches [26] in experiments during IMT provides direct evidence for interactions. Moreover, both our deep learning classifier [27] and the critical exponents reported by us for avalanches [28] further indicate that interactions are necessary in order to explain the morphology of the domains. Since our previous defect motion model did not include these interactions, it could not reproduce avalanche phenomena. These insights motivate the introduction of such interactions into our current model, significantly extending the foundations laid in our earlier work. In this work, we show that these interactions increase the hysteresis width (which now better matches the hysteresis observed in experimental curves) and explain the peak in RRM vs. turnaround temperature, initially observed in transport [22] and reported here for the first time in optics. Furthermore, with this working model in hand, we predict that interactions also lead to a marked enhancement of the RRM effect.

2 | Models and Methods

Here, we develop an Interacting Defect Motion Model to describe the thermally driven evolution of the spatial distribution of the memory effect in TMOs. This model combines two key physical mechanisms: (1) the diffusion and segregation of point defects that locally modify transition temperatures, and (2) the cooperative interactions between metallic and insulating domains that produce avalanche behavior and hysteresis. We begin by reviewing our previously developed defect motion framework, then introduce the Random Field Ising Model that captures domain interactions. To generate realistic initial conditions without relying on experimental data, we employ correlated random fields that reproduce the spatial heterogeneity observed in real samples. These components are then integrated into the Interacting Defect Motion Model that couples defect redistribution with domain dynamics. This coupled approach reproduces the full width of experimental hysteresis loops, eliminates dependence on experimental transition temperature maps (T_c) as inputs, and predicts how interaction strength controls the magnitude of the RRM effect. Finally, we describe the experimental methods used to validate our theoretical predictions.

2.1 | Defect Motion Model

To account for the spatial variations in the T_c map observed in our previous work—where T_c increases in some regions and decreases in others as a result of the RRM process, and moreover T_c changes throughout the entire sample rather than only at scars (see figure S7 in ref. [25])—we proposed that the local T_c change is influenced by the change of defect density ρ at each site i:

$$\Delta T_c^{(i)} = -\alpha \Delta \rho_i \tag{1}$$

The evolution of the defect density is then modeled using the 2D diffusion-segregation equation [29]:

$$\frac{\partial \rho(\boldsymbol{r}, t)}{\partial t} = \nabla \left[D \left(\nabla \rho - \frac{\rho}{\rho_{\mathrm{eq}}} \nabla \rho_{\mathrm{eq}} \right) \right], \tag{2}$$

where $D = D(\sigma_{\boldsymbol{r}}, T)$ is the diffusion coefficient with binary phase indicator σ, and $\rho_{\mathrm{eq}} = \rho_{\mathrm{eq}}(\boldsymbol{r})$ is the equilibrium density, assigned two distinct values within the metallic and insulating regions. To prevent non-physical behavior near the phase boundary, we apply

Gaussian smoothing to the segregation current of defects (See Supporting Information). The additional term involving $\nabla \rho_{\text{eq}}$ in Equation (2), compared to the well-known diffusion equation, arises from the nonuniform chemical potential near the metal–insulator phase boundaries. This term becomes significant near phase boundaries as indicated in Figure 2 and vanishes deep inside the metallic or insulating regions. The ratio of the equilibrium defect density deep inside two phases $\rho_{\text{eq}}^{\text{insulator}}/\rho_{\text{eq}}^{\text{metal}} = s$ is known as the "segregation coefficient". See Supporting Information for full details.

2.2 | Correlated Random Field Ising Model

The collective behavior of the metallic and insulating domains is described by the Correlated Random Field Ising Model (C-RFIM), which incorporates both nearest-neighbor interactions and spatially correlated disorder. In this subsection we introduce the C-RFIM we used in this work by breaking it down to more fundamental ideas.

2.2.1 | Random Field Ising Model

The Random Field Ising Model (RFIM) provides a theoretical framework for describing hysteretic phase transitions in systems with quenched disorder [30]. The model consists of a lattice of Ising spins that are coupled via nearest-neighbor interactions and are subjected to site-dependent random local fields. Competition between the ordering tendency of the ferromagnetic interactions and the disordering effect of the random fields is responsible for the model's complex behavior, including hysteresis and avalanches.

The total energy of the system is given by the RFIM Hamiltonian:

$$H = -J \sum_{\langle i,j \rangle} \sigma_i \sigma_j - \sum_i (h_i + h_{\text{ext}}) \sigma_i \tag{3}$$

Here, the first term describes the nearest-neighbor interaction of strength J, which favors alignment of adjacent spins. The second term accounts for the energetic contributions of the local random field h_i drawn from independent identical standard Gaussian distributions ($h_i \sim \mathcal{N}(0,1)$) and the uniform external field h_{ext} on each spin σ_i.

The RFIM quantitatively reproduces key experimental signatures of the IMT in TMO materials, by mapping metallic and insulating regions to Ising pseudospins $\sigma = +1$ and $\sigma = -1$, respectively. A prominent feature of the model is the occurrence of avalanches, abrupt, collective transformations of multiple domains in response to a small change in the external field, which are observed experimentally. As discussed in the Introduction, avalanches in VO_2 [25, 26] and in V_2O_3 [31] indicate the presence of interactions in the system. The model also intrinsically displays hysteresis, where the width of the hysteretic loop is determined by the strength of the random field distribution, corresponding to the degree of material disorder.

As in ref. [28], we map experimental temperature T to the uniform external field h_{ext} that drives the transition from insulator to metal. Moreover, Our previous machine learning classification [27] indicates that the metal/insulator domain maps of VO_2 thin film belong to the universality class [32] of the two-dimensional (2D) Random Field Ising Model. To capture the spatial stochasticity observed in experimental T_c maps [25], there must be a random field assigned at each site i as follows:

$$H = -J \sum_{\langle i,j \rangle} \sigma_i \sigma_j - \sum_i f\left(T - T_c^{(i)}\right) \sigma_i \tag{4}$$

The function f is a monotonic increasing function satisfying $f(0) = 0$. The term $T_c^{(i)}$ represents the local critical temperature at site i, generated from a correlated random field as described in the next section. Here, $f(T - T_c^{(i)})$ acts as an effective external field that biases the local Ising variable σ_i toward a particular state.

2.2.2 | Correlated Random Field

Figure 1a shows an example of an experimentally derived map of the local transition temperature T_c. Here, we have imaged the metal-insulator phase separation state on a thin film of VO_2 during the warming branch of the initial major hysteresis loop (ML1-W) using high-resolution optical microscopy. By slowly heating the sample from a fully insulating state to a fully metallic state, we record the T_c at each pixel (see Figure 1a) to produce a T_c map through the DOMain INtensity Overturn (DOMINO) procedure we introduced in Basak et al. [25].

In order to create a purely theoretical model, we use initial T_c maps that are generated by statistical means, to have similar statistics and spatial correlation characteristics to those observed experimentally. The T_c map Figure 1a indicates random field behavior, with regions of high and low critical temperatures extend over a range of length scales, demonstrating inherent spatial correlations rather than uncorrelated disorder (see the Supporting Information). This correlation necessitates the use of a correlated random field, rather than an uncorrelated Gaussian random field typically used in the RFIM.

Therefore, to create the initial theoretical T_c map, we first construct an uncorrelated random field with independent identical standard Gaussian distributions. Then we apply Cholesky decomposition (see the Supporting Information) to transform the uncorrelated random field into a spatially correlated random field. Finally, to account for experimental conditions, we apply Gaussian blurring to the correlated random field. Figure 1b shows a T_c map in theory with Gaussian blurring applied, which reproduces the smoothing effect observed in optical measurements in Figure 1a (see the Supporting Information for detailed comparison).

This initial theoretical T_c map is considered a replacement of the experimental maps with minimal assumptions. By using the initial theoretical T_c map as new model inputs, we eliminate data dependence and enable a more self-consistent theoretical description of RRM. Note that the RRM temperature protocol (see below) will ultimately modify this initial T_c map.

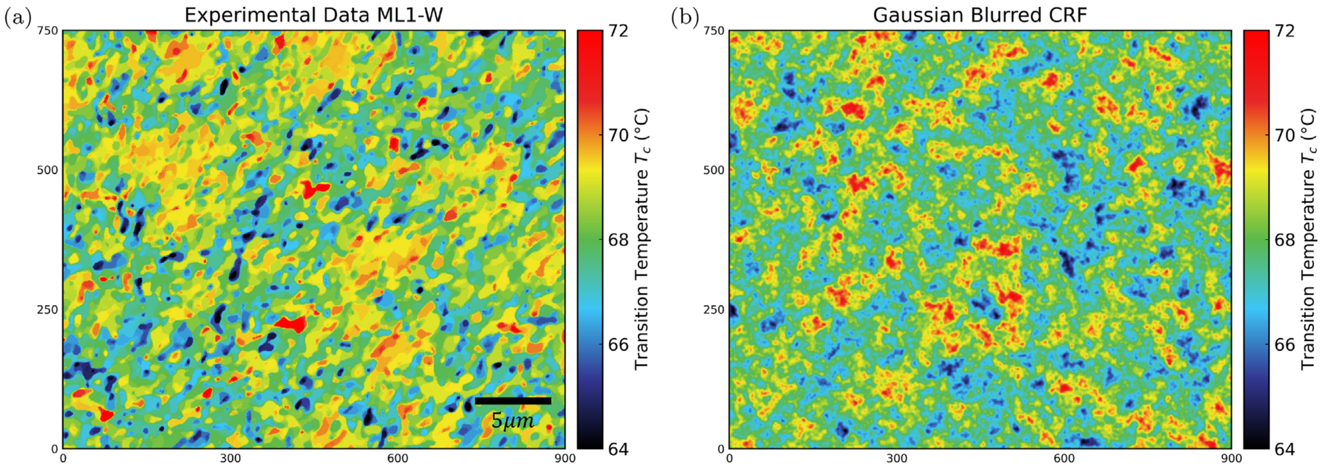

FIGURE 1 | (a) Experimental T_c map measured during the first warming process. (b) Theoretical T_c map using correlated random field (CRF) with Gaussian blurring effect to facilitate comparison with the experimental resolution of the T_c map in Panel (a).

2.3 | Dynamics of Defect Motion with C-RFIM

In the presence of both defect motion and Ising-type interactions via the C-RFIM, the simulation proceeds on a square lattice, as illustrated in Figure 2. Each lattice site represents a pixel in the experimental images, associating with three local properties that evolve over time: the Ising variable σ_i denoting whether the site is insulating or metallic, the local critical temperature $T_c^{(i)}$, and the local defect density ρ_i. The simulation proceeds through the following steps:

1. Calculate the defect distribution using the diffusion-segregation equation [Equation (2)].
2. Compute the critical temperature at each site based on the local defect density using Equation (1).
3. Update the second term of RFIM [Equation (4)] to reflect the new critical temperatures.
4. Update the non-equilibrium Ising variable σ_i configuration of the C-RFIM. Employ the checkerboard update method to iteratively update the pseudospins, accepting new configurations that lower the system's energy until it reaches a local minimum.
5. Update the equilibrium defect density ρ_{eq} and the diffusion coefficients based on the updated pseudospin variables.

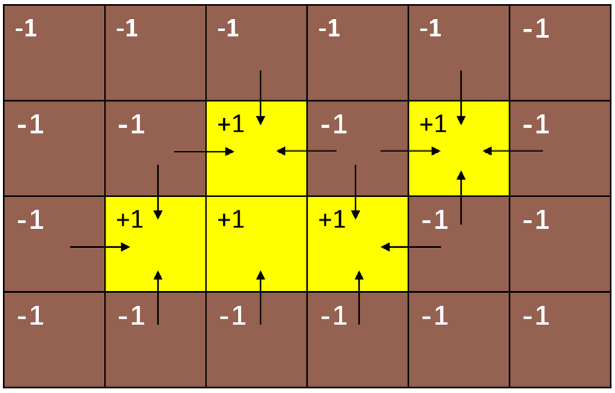

-1	-1	-1	-1	-1	-1
-1	-1	+1	-1	+1	-1
-1	+1	+1	+1	-1	-1
-1	-1	-1	-1	-1	-1

FIGURE 2 | Schematic representation of a portion of the lattice used in the simulation. Arrows indicate the defect current driven by the gradient of chemical potential. Labels with Ising variable +1 and −1 represent metallic (yellow) and insulating (brown) regions, respectively. In the mixed phase, defects concentrate preferentially in metallic regions.

These steps collectively constitute one iteration of our simulation process.

2.4 | Experimental Methods: Thin Film Preparation and Optical Setup

Our simulations will be compared to optical Ramp Reversal Memory measurements of a VO_2 film (100 nm) epitaxy on an r-cut sapphire substrate. This one was prepared by reactive RF magnetron sputtering of a V_2O_3 target (using a 99.9% pure powder from Noah Industries). A mixture of ultrahigh purity (UHP) argon and UHP oxygen was used for sputtering. The total pressure during deposition was 3.4 mTorr, and the oxygen partial pressure was optimized to 0.26 mTorr (8% of the total pressure). The substrate temperature during deposition was 480 °C while the RF magnetron power was kept at 100 W. Grain size in these films are typically found to be 40 nm to 130 nm in 100 nm to 150 nm films [33]. X-ray diffraction showed the textured VO_2 film growth along the (200) monoclinic (low-temperature phase of VO_2) or (011) rutile (high-temperature phase of VO_2) direction (see the Supporting Information). 35 μm width VO_2 ribbons were patterned using reactive ion etching Ar/Cl_2 environment. Gold electrodes (20 nm Ti)/(100 nm Au) were deposited on top of the film separated by 30 μm. Resistance temperature measurements reveled an abrupt, four-order-of-magnitude IMT around 68 °C, which attest to the proper stoichiometric composition of the synthesized thin films (see the Supporting Information). Using autofocused, auto-aligned series of images of the surface of VO_2, we track the metal-insulator patches down to optical wavelength resolution throughout the transition. This allowed us to map the critical temperature T_c of the sample in Figure 1a, the average grayscale intensity vs. temperature (Figure 4) and the ramp-reversal memory change as a function of the reversal

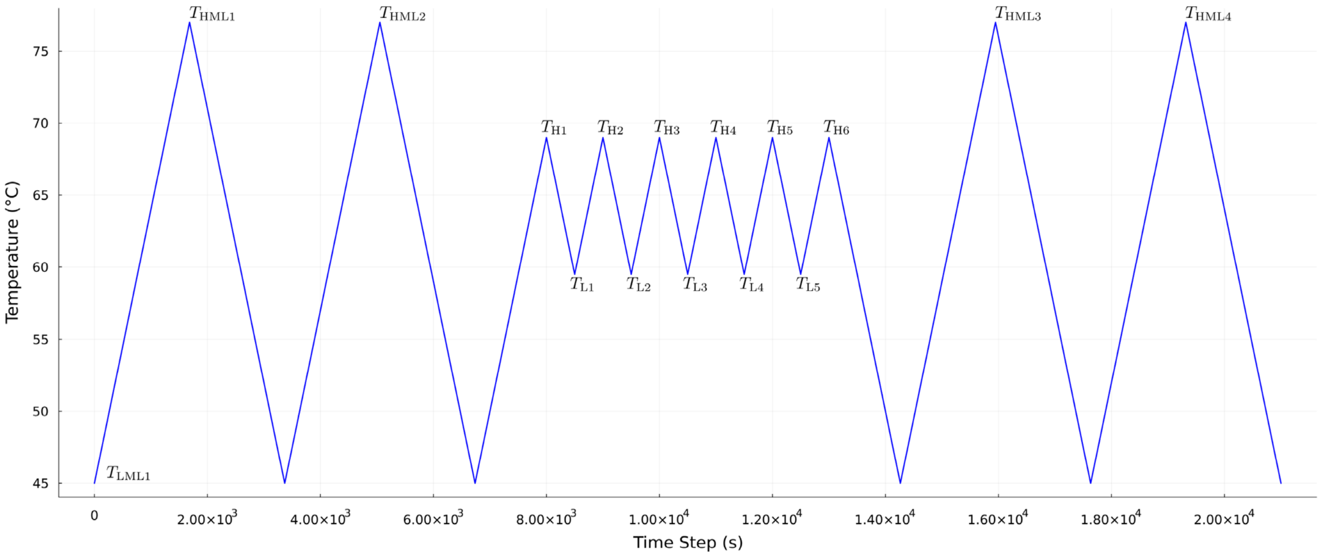

FIGURE 3 | (a) Schematic ramp reversal temperature protocol used in our simulation and experiment.

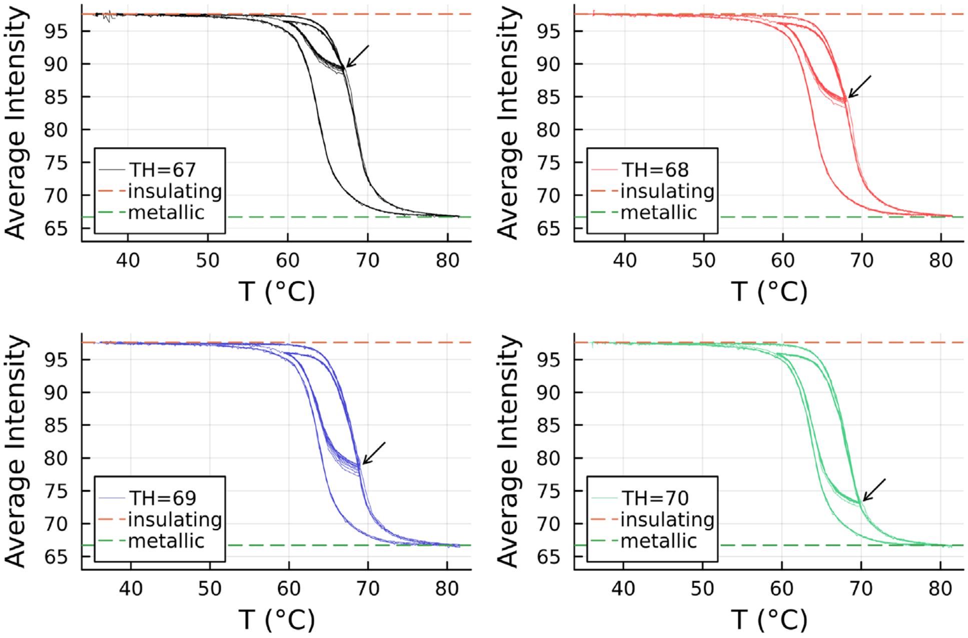

FIGURE 4 | Experimental hysteresis loops measuring average grayscale intensity during the temperature protocol of ref. [25] (similar to Figure 3). As subloops are performed, the average grayscale of the sample rises progressively (see arrows), at different rates in each panel. This rise is the basic ramp reversal memory effect, previously reported for a single T_{H} (68 °C) and now observed at multiple T_{H} values (67 °C, 68 °C, 69 °C, and 70 °C) around the IMT warming inflection point.

temperature T_{H} (Figure 8). Full details of sample preparation, characterization, and the optical setup can be found in previous papers [25, 34].

3 | Results and Discussion

In this section, we present our simulation results that model the memory effect observed in VO_2 and discuss the underlying mechanisms. We hypothesize that the memory effect emerges from the interplay between point defect diffusion and the interactions inherent in the IMT itself. To test this hypothesis, we simulate the metal–insulator coexistence region under a specified temperature protocol (Figure 3) designed to replicate the conditions of ramp-reversal experiments. Our simulations reproduce the temperature-dependent behavior of RRM observed experimentally in VO_2, thereby providing strong support for our theoretical framework.

3.1 | Hysteresis Loop of VO_2

Figure 4 shows the spatially averaged 8-bit grayscale optical reflectivity intensity versus temperature of VO_2 obtained during the ramp reversal protocol of ref. [25] under different T_{H} configurations. We observed that VO_2 becomes progressively more insulating at temperature T_{H} after consecutive subloop thermal cycling, indicating an effective increase of T_c. This high effective T_c persists during the following major-loop thermal cycle, but it is erased in the final major-loop cycle once the sample is heated to high temperatures (successive surface maps showing the detailed locations where the sample's metal–insulator patches change as memory is encoded are presented in Figure S6). This reversible T_c modification constitutes the RRM effect [22, 25]. As discussed further, we used these experimental data to verify the performance of our defect-motion and C-RFIM models.

To simulate the hysteresis behavior of VO_2, we employed a temperature protocol (Figure 3) similar to that used in ref. [25]. This protocol consists of two full hysteresis loops, called major loops, followed by six subloops and then two additional major loops. Figure 5a shows the result of our previous model [25] using above protocol, where the width of hysteresis loops is nonphysically small. Utilizing the C-RFIM as described in Equation (4) without incorporating defect diffusion, we obtained the hysteresis loop shown in Figure 5b, which reproduces the hysteresis behavior of VO_2 during a full temperature loop.

The complete Defect Motion Model with C-RFIM is depicted in Figure 5c. Note that by setting the interaction strength to zero ($J = 0$), the full model reduces to our previous non-interacting defect motion model shown in Figure 5a. Conversely, by nullifying the influence of defect motion on the local T_c (by setting $\alpha = 0$), the model reduces to the pure C-RFIM without the RRM effect, shown in Figure 5b.

The outer loops in Figure 5 represent the major loop of the temperature protocol in Figure 3. In this loop, the sample is heated from a fully insulating state to a fully metallic state and then cooled back to the fully insulating state. The inner loops correspond to the subloops, where the sample starts from the insulating state at a temperature T_{L}, is heated up to a temperature T_{H} within the phase coexistence region, and then cooled back to T_{L}.

3.2 | Ramp Reversal Memory

When defect motion is introduced into the C-RFIM, ramp reversal memory emerges during the subloops [25]. As depicted in Figure 5c, the subloops exhibit a counter-clockwise rotation with a decaying increment due to the dynamics of defects. After six subloops, the subsequent major loop (ML3) shows a significant increase in the insulating area at temperatures near T_{H}. If additional major loops are executed after these subloops, the RRM effect is gradually erased, and the hysteresis loop eventually returns to the shape observed in the initial major loop (ML1).

Note that within the Defect Motion Model (with or without C-RFIM), the defect density movement that happens during the RRM protocol becomes reset when the material is held at high temperature in the uniform phase. In this sense, the RRM in this model does not suffer from fatigue [35].

The physical mechanism underlying RRM in our model is that when the sample is in the mixed phase having both metal and insulator domains, the thermodynamic tendency is for the metallic regions to have a higher defect concentration than the insulating regions. This mechanism is similar to the floating melting zone refinement method for removing impurities from a crystal (for detailed microscopic explanations, see the Supporting Information of ref. [25]). This means that during the subloops, as metal repeatedly expands and recedes, it carries with it a higher concentration of defects each time. The main driving force is different equilibrium defect densities in metallic versus insulating regions. This redistribution locally modifies the critical temperature according to Equation (2), creating a "memory" of the thermal cycling history. With repeated minor loops, defects accumulate in certain regions progressively, enhancing the memory effect. However, when the sample undergoes a full major loop and becomes completely metallic, the defects can redistribute in a more uniform way throughout the sample, gradually resetting the accumulated memory and restoring the original hysteresis behavior. The interactions introduced in Equation (4) have an indirect effect on the defect density through the morphology of the domains, set by a combination of interactions and local random field effects.

3.3 | Parameter Dependence of the RRM Effect

Our model indicates that the magnitude of the maximum RRM effect depends on the highest temperature T_{H} reached during the subloops such that T_{H} can be optimized to maximize the RRM effect. Figure 6 shows the change in relative insulating area before and after the subloops, $\Delta A(T) = A_{\mathrm{ML3}}(T) - A_{\mathrm{ML2}}(T)$. A peak in the change in relative insulating area before and after the subloops happens with or without interactions. In the non-interacting case (Figure 6a), the curves appear smooth, since Ising interactions that lead to avalanches are absent. Introducing interactions ($J \neq 0$) enhances the RRM effect, and also introduces jaggedness in the curves due to these avalanches, as shown in Figure 6b.

To quantify the RRM effect, we define key parameters from the temperature-dependent area change curves in Figure 6. For each curve, we identify the peak position (marked with a red dot in Figure 7) to define T^{peak} as the temperature at which the peak occurs and $\Delta A^{\mathrm{peak}} = \max(\Delta A(T))$ as the maximum change in insulating area.

3.3.1 | Magnitude of Maximum RRM Effect

We perform systematic simulations across different values of J and T_{H} using our temperature protocol. For each parameter set, we calculate the difference between major loops immediately before and after the subloops as shown in Figure 6, extract ΔA^{peak} from the resulting curves as defined in Figure 7, and plot the data using $(J, T_{\mathrm{H}}, \Delta A^{\mathrm{peak}})$ triplets. The results are shown in Figure 8a. Our results reveal that not only is there a peak in the RRM effect as a function of T_{H}, but that *interactions amplify the RRM*

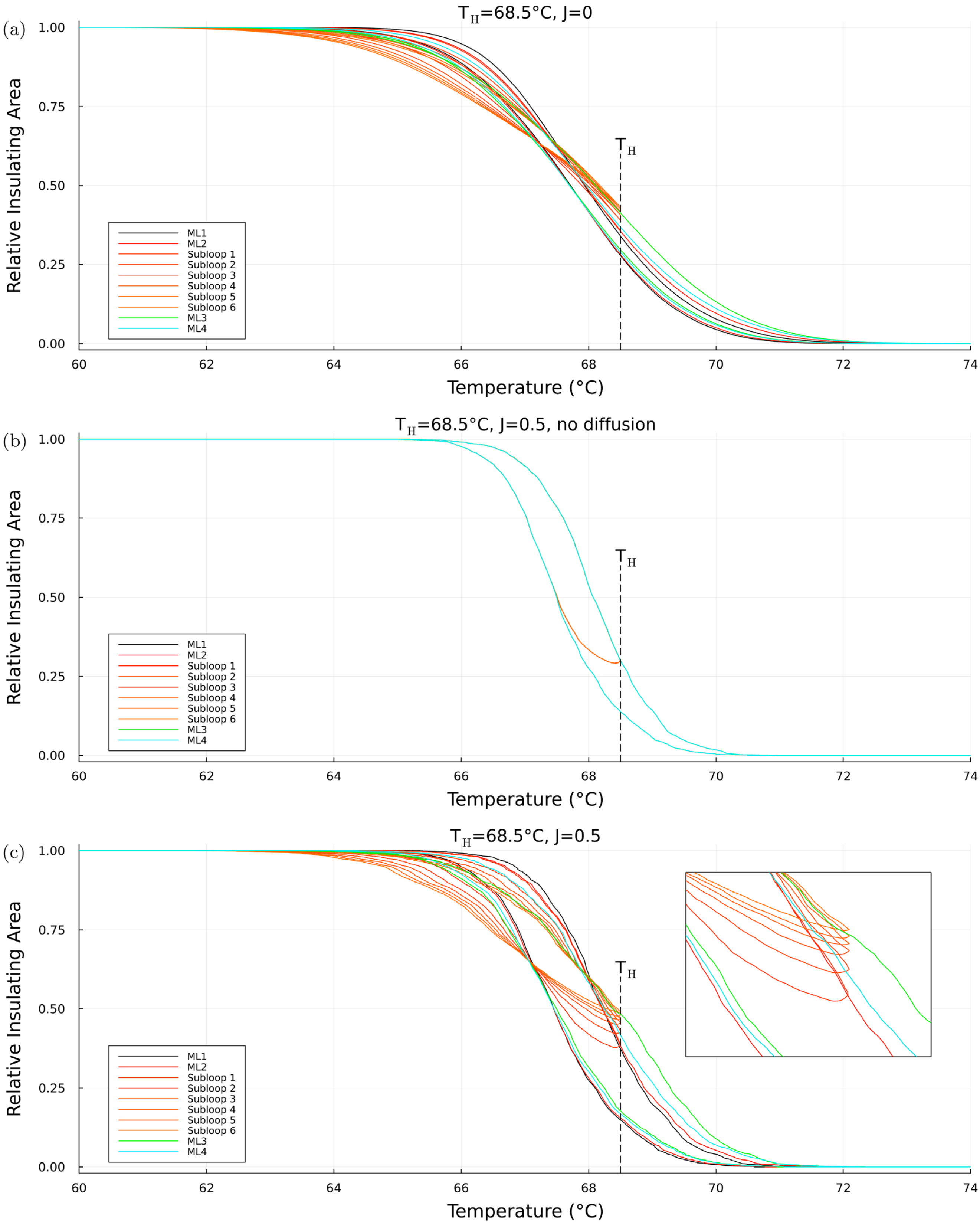

FIGURE 5 | Simulated hysteresis loops of the model under different conditions. The black curve represents the initial major hysteresis loop (ML1), while the yellow curve corresponds to the final major loop (ML4) after six subloops. The progression from dark red to orange to yellow indicates the sequence of the loops. (a) Results with defect motion but without interactions ($J = 0$). (b) Results with interactions ($J = 0.5$) but without defect motion. Loops stack on top of each other since there is no RRM effect. (c) Results with both defect motion and interactions ($J = 0.5$) included. Each successive subloop is rotated counter-clockwise from the previous one.

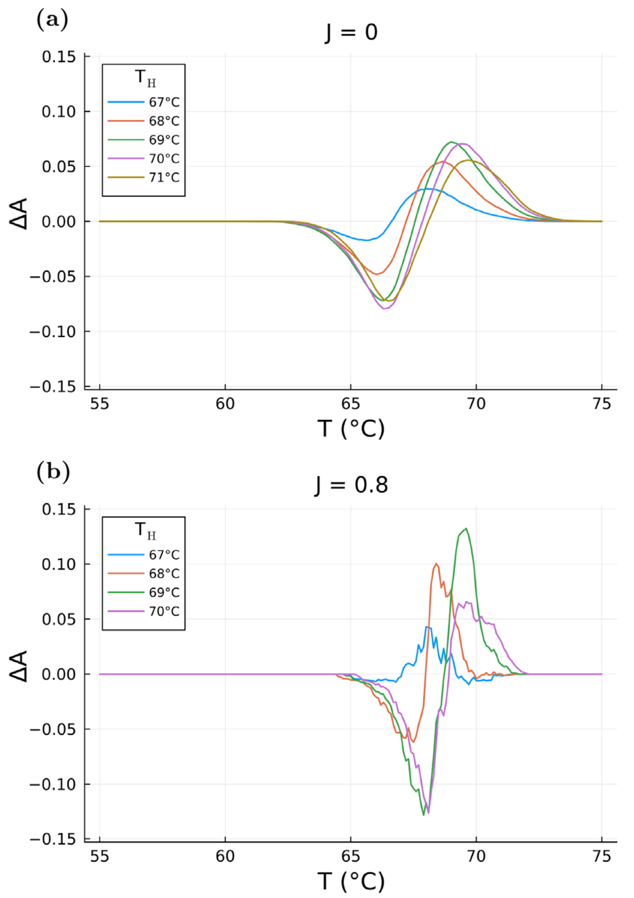

FIGURE 6 | Simulated curves of fractional area change versus temperature during the warming process. The difference of two heating curves $\Delta A(T) = A_{\mathrm{ML3}}(T) - A_{\mathrm{ML2}}(T)$ is plotted, where A is the fraction of insulating area from Figure 5. There are six temperature reversal subloops between Major Loop 2 and Major Loop 3, as shown in Figure 3. (a) Without interactions ($J = 0$), resulting in smoother curves. (b) With interactions ($J = 0.8$), showing jaggedness due to avalanches, as well as enhanced memory due to interactions.

effect. Specifically, as interaction strength is increased the RRM effect grows in intensity, and the peak of the RRM effect as a function of T_{H} becomes more pronounced. This result reveals that interactions fundamentally change how memory accumulates. Without interactions, metal-insulator phase boundaries move gradually and continuously, creating defect depletion regions just outside of each metallic domain. The depletion region both raises the local T_c (making it harder for metal to advance there in subsequent warming ramps), and slows the flow of defects across the boundary, limiting the RRM effect. However, we hypothesize that because interactions enable avalanches, boundaries can jump over depletion regions, allowing higher defect current across phase boundaries and increasing the memory accumulation during subloops.

We note that we observe the emergence of a possible double-peak structure in the relationship between the maximum RRM effect and T_{H} (Figure 8a). However, further investigation is needed to confirm the robustness of this double-peak feature, as it might be sensitive to the specific realization of the correlated random field and associated noise.

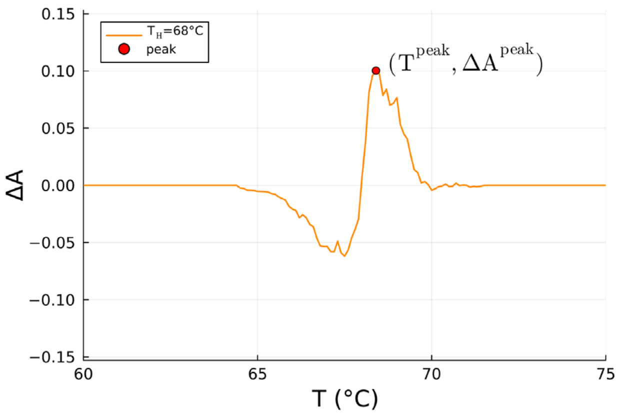

FIGURE 7 | Definition of T^{peak} and ΔA^{peak}. The red point shows corresponding peak position for $T_{\mathrm{H}} = 68\,°\mathrm{C}$.

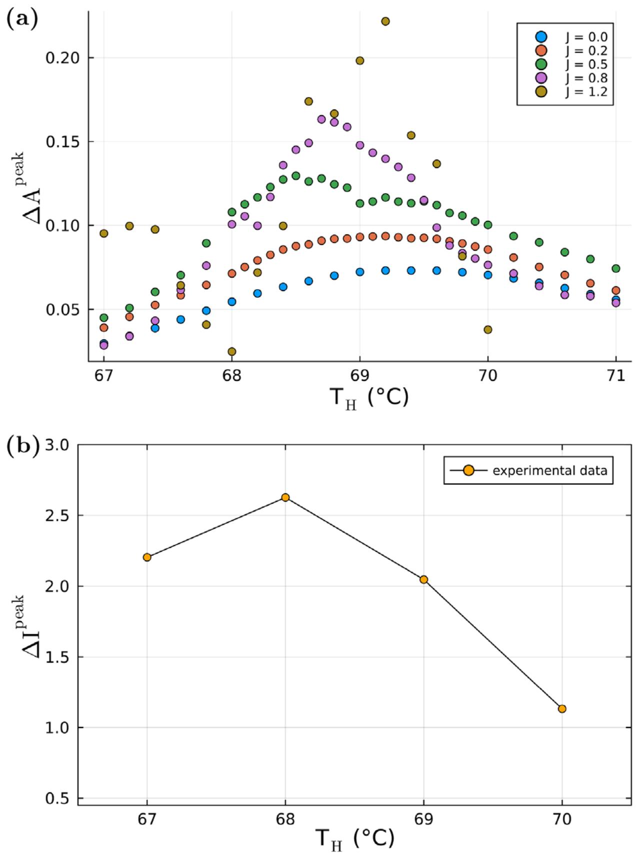

FIGURE 8 | (a) Simulated RRM effect versus T_{H}; (b) Experimental optical data of RRM effect versus T_{H}. Note that in both theory and experiment, we find a peak in the magnitude of the RRM effect as a function of T_{H}.

In Figure 8b, we plot the maximum RRM effect vs. T_{H} derived from experiment, measured via reflected light using a CCD camera, derived from Figure 4. We quantify the RRM effect in terms of the maximum difference in the average intensity I of reflected light, comparing major loops measured immediately before and immediately after the temperature subloops: $\Delta I^{\mathrm{peak}} = \max(\Delta I(T))$, where $\Delta I(T) = I_{\mathrm{ML3}}(T) - I_{\mathrm{ML2}}(T)$. Additional details from the experiment are provided in the Supporting Information, including color-coded VO_2 sample maps showing the spatial

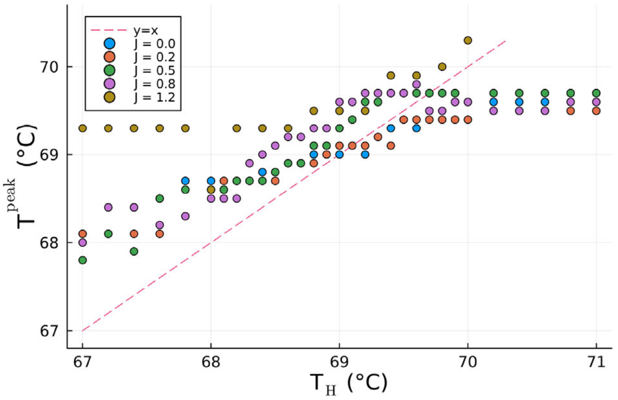

FIGURE 9 | Simulated optimal temperature T^{peak} for each T_{H}, as illustrated in Figure 7. The dotted purple line is a guide to the eye.

distribution of RRM encoding. Note the agreement between theory and experiment: In both cases, we find that there is a peak in the magnitude of the RRM effect as a function of the subloop turnaround temperature T_{H}. this is the first time it has been reported in optics.

3.3.2 | Optimal Temperature T^{peak} for Maximum RRM Effect

The optimal temperature for achieving the maximum RRM effect, denoted as T^{peak}, also exhibits a clear dependence on T_{H} (Figure 9). Our simulations reveal that T^{peak} closely tracks T_{H} for $T_{\text{H}} < 70\,^{\circ}\text{C}$ and saturates as T_{H} approaches the temperature at which the hysteresis loop closes. This observed temperature dependence suggests that the defect distribution established by repeated movement of domain walls at T_{H} plays a crucial role in facilitating the memory effect. It corroborates findings from previous studies [23] and aligns with our experimental observations.

3.3.3 | Optimal Subloop Turnaround Temperature T_{H}

Since T_{H} is a readily controllable parameter in experiments, understanding its influence on the RRM effect is paramount for optimizing device performance. Our results show that as the interaction strength J increases, the optimal T_{H} for maximizing the RRM effect approaches the inflection point of the warming branch of the initial major hysteresis loop (ML1-W), as illustrated in Figure 10. This provides a valuable guideline for experimentalists seeking to maximize the RRM effect: the subloops should be designed such that T_{H} is near the inflection point of the major loop's warming branch.

The roughly linear relationship observed in Figure 10 for moderate to strong interactions can be understood by considering the total perimeter between metallic and insulating domains. As shown in Figure 11, the system exhibits a maximum in the total metal–insulator boundary length near the inflection point of the warming branch. Since the defect movement responsible for the RRM effect increases with boundary length, maximizing the duration of the subloops near the inflection point promotes enhanced memory accumulation. At temperatures significantly below the inflection point, memory accumulation is slow due to the limited interfacial area. Conversely, at temperatures significantly above the inflection point, the established memory effect is diminished by defect diffusion and the reduction in the minority phase. The combined effect results in an optimal turn-around temperature, $T_{\text{H}}^{\text{opt}}$, that sits near the inflection point.

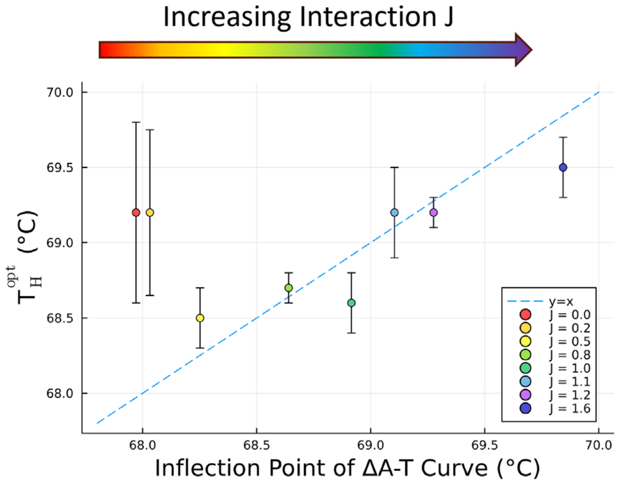

FIGURE 10 | Optimal T_{H} versus the inflection point of the warming branch of Major Loop 2, extracted from the simulation data. Error bars indicate the precision of finding $T_{\text{H}}^{\text{opt}}$ from Figure 8a. They are derived from the peak widths in Figure 8a, and set by the range of T_{H} values where $\Delta A^{\text{peak}}(T_{\text{H}}) > 0.95\Delta A^{\text{peak}}(T_{\text{H}}^{\text{opt}})$. For moderate to strong interactions, the inflection point increases with increasing J. The dotted blue line is a guide to the eye.

It is crucial to distinguish between different definitions of the "inflection point". The relevant inflection point for maximizing RRM, as described above, is that of the insulator-metal fraction versus temperature curve. This can be determined by tracking the grayscale in optical data [25,34]. For data used in Figure 10, we determine these inflection points by fitting the relative insulating curve with a hyperbolic tangent function. However, the inflection point commonly reported in the literature is deduced from resistivity. This one can be misleading, as it can in principle be shifted with respect to the insulator-metal fraction due to complex percolation paths in the sample.

3.4 | What Our Model Does Not Capture

When comparing our theoretical results to experimental observations, we find that while our simulations capture several key features observed experimentally, certain discrepancies are present. Specifically, in Figure 5c, our simulations show a decrease in the insulating area at low temperatures, which is not seen in experimental hysteresis loops in Figure 4. This discrepancy may arise from our assumption that the total number of defects is conserved and that changes in T_c depend linearly on variations in the defect density ρ. Our assumption leads to a sum rule $\left(\sum_i \Delta T_c^{(i)} = -\alpha \sum_i \Delta\rho_i = 0\right)$. Consequently, if a portion of the hysteresis curve shifts upward, another portion must shift downward, which differs from experimental observations where the curves primarily shift upward. In fact, density functional

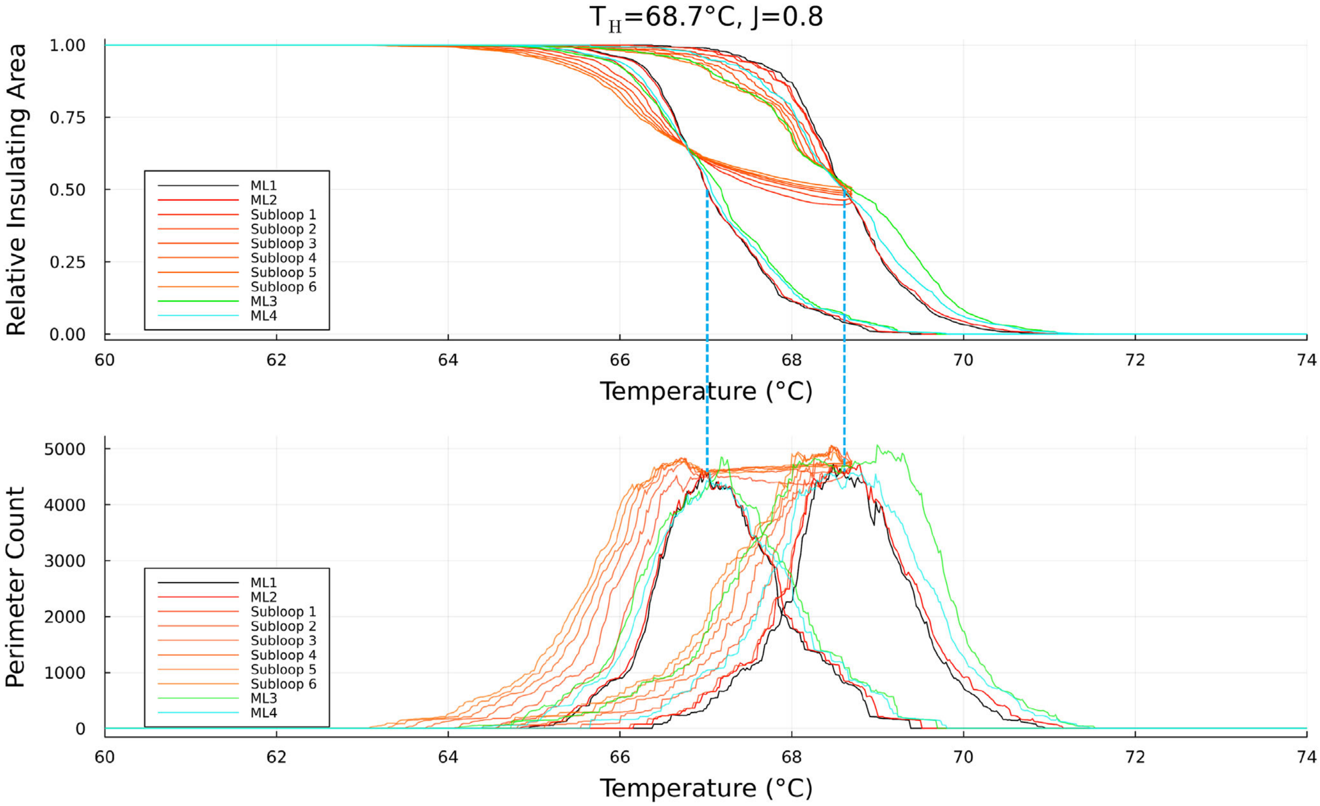

FIGURE 11 | Comparison of temperature-dependent phase transition behaviors, showing the relationship between the metallic/insulating area fraction and the total metal-insulator boundary length (perimeter) at $J = 0.8$, $T_H = T_H^{\mathrm{opt}}(J = 0.8) = 68.7$ (purple dot in Figure 10). Vertical dashed lines indicate the inflection points of the warming (right line) and cooling (left line) branches of the hysteresis loop, corresponding to the temperatures at which the total metal-insulator boundary length is maximized. In the absence of interactions, the perimeter curve would be approximately proportional to the absolute value of the derivative of the relative area curve.

theory calculations indicate that the defects in VO_2 are most likely oxygen vacancies and interstitials [36], whose concentrations depend on temperature. Since the experiments are carried out with the samples exposed to the air, it seems reasonable that oxygen vacancies and interstitials should change with temperature. At lower temperatures, a reduction in defect density could, for example, counteract the downward shift of the hysteresis curve in the low-temperature regime. We leave the exploration of this effect to future work. Another possibility involves non-point defects, such as phase boundaries and strain fields, which may increase the local critical temperature.

It should also be noted that while our model of defect diffusion within dynamic interacting phase separated domains includes certain phenomenology of the scar model (that significant local action happens at phase boundaries), our model also includes phenomenology that goes beyond the expectations of the scar model, including: (1) Memory accumulates throughout the entire bulk of the sample, and (2) Whereas some regions will have increased local transition temperature, some other regions will have decreased local transition temperature. Future work may also consider integrating our defect motion model with the scar model proposed by Vardi et al. [22], with the goal of developing a more comprehensive theoretical framework.

3.5 | Future Outlook and General Applicability

Our model makes minimal assumptions: that phase separated domains interact, and that for thermodynamic reasons point defects preferentially gather in one type of domain over the other. As a result, our theoretical model predicts that RRM should be a general phenomenon in materials undergoing patterned electronic phase separation, as conjectured in ref. [24]. This is consistent with the fact that the RRM effect has been seen in a variety of TMO's, including VO_2 as discussed extensively here, as well as V_2O_3 and $NdNiO_3$ [22,23]. The minimal assumptions of our theoretical model imply that the RRM phenomenon should be far more widespread, and should be observable in materials with locally phase separated electronic domains (as recently found in 1T-TaS_2 [24]). Potential candidates include: cuprate high temperature superconductors, some of which have shown regimes of interleaved phase separated regions of superconducting and non-superconducting domains [37, 38]; graphene [39], strontium iridates [40, 41], 2DEG superconductors [42, 43], manganites [44], and even iron-based superconductors [45]. In the low disorder strength limit of random field Ising models, the hysteresis width is proportional to the interaction strength. Therefore, we predict that samples with the largest hysteresis width are the best candidates for strong RRM.

4 | Conclusion

In order to address the experimental findings not fully explained by the scar model, we developed the non-interacting defect motion model in our previous work. This model successfully reproduced several key observations, including decreased T_c values and RRM effects that accumulate deep inside metal/insulator patches. However, due to the lack of interactions among metal and insulator domains, it did not include avalanche physics and the hysteresis loops were not very wide. To improve our theoretical framework, we have coupled the defect motion model with a Correlated Random Field Ising Model (C-RFIM) on a site-by-site basis. Introducing Ising interactions provides several major advantages that transform our model from a qualitative explanation to a quantitative predictive tool. First, the interacting model successfully reproduces the complete experimental hysteresis width (Figure 5c) and captures avalanche behavior evident in the jaggedness of Figure 6b, which the non-interacting model cannot reproduce. Most significantly, we discover that interaction strength directly controls memory performance: increasing the nearest-neighbor interaction J dramatically enhances the maximum RRM effect (Figure 8a). This discovery provides a clear pathway for optimizing memory devices through material parameters that control effective interaction strength. Notably, our interacting model predicts that the maximum RRM effect occurs near the inflection point of the warming process, consistent with the optical measurements on VO_2 reported here.

By incorporating both defect dynamics and interactions between metallic and insulating domains, our model captures more features of the overall hysteresis behavior and provides valuable insights into the underlying mechanisms driving these phenomena. These findings not only advance our fundamental understanding of RRM but also establish a theoretical foundation for developing more effective memory devices, neuromorphic computing applications, and other potential technologies based on IMT materials. Moreover, the minimal assumptions of our theoretical model imply that the RRM effect should be a generic phenomenon in materials exhibiting local electronic phase separation, opening new avenues for searching for new quantum materials that exhibit unconventional memristive properties.

Acknowledgements

The authors acknowledge helpful conversations with K. A. Dahmen and A. Sharoni. E.W.C. acknowledges support from NSF Grant No. DMR-2006192 and from a Fulbright Fellowship, and thanks the Laboratoire de Physique et d'Étude des Matériaux (LPEM) at École Supérieure de Physique et de Chimie Industrielles de la Ville de Paris (ESPCI) for hospitality. E.W.C. and Y.S. acknowledge support from DOE BES Award No. DE-SC0022277. This research was supported in part through computational resources provided by Research Computing at Purdue, West Lafayette, Indiana [46]. The work at UCSD (PS, IKS) was supported by the "Quantum Materials for Energy Efficient Neuromorphic Computing" (Q-MEEN-C), an Energy Frontier Research Center funded by the U.S. Department of Energy, Office of Science, Basic Energy Sciences under the Award No. DE-SC0019273. The work at ESPCI (M.A.B., L.A., and A.Z.) was supported by Cofund AI4theSciences hosted by PSL University, through the European Union's Horizon 2020 Research and Innovation Programme under the Marie Skłodowska-Curie Grant No. 945304.

Conflicts of Interest

The authors declare no conflicts of interest.

Data Availability Statement

The data that support the findings of this study are available from the corresponding author upon reasonable request.

References

1. C. López, "Artificial Intelligence and Advanced Materials," *Advanced Materials* 35, no. 23 (2023): 2208683.

2. P. Salev, L. Fratino, D. Sasaki, et al., "Magnetoresistance Anomaly During the Electrical Triggering of a Metal-Insulator Transition," *Physical Review B* 108, no. 17 (2023): 174434.

3. C. Feng, B.-W. Li, Y. Dong, et al., "Quantum Imaging of the Reconfigurable VO_2 Synaptic Electronics for Neuromorphic Computing," *Science Advances* 9, no. 40 (2023): eadg9376.

4. A. Zimmers, L. Aigouy, M. Mortier, et al., "Role of Thermal Heating on the Voltage Induced Insulator-Metal Transition in VO_2," *Physical Review Letters* 110, no. 5 (2013): 056601.

5. I. Boybat, M. Le Gallo, S. R. Nandakumar, et al., "Neuromorphic Computing with Multi-Memristive Synapses," *Nature Communications* 9, no. 1 (2018): 2514.

6. T. Ahmed, "Bio-inspired artificial synapses: Neuromorphic Computing Chip Engineering with Soft Biomaterials," *Memories - Materials, Devices, Circuits and Systems* 6 (2023): 100088.

7. R. Khan, N. U. Rehman, S. Iqbal, S. Abdullaev, and H. M. Aldosari, "Resistive Switching Properties in Memristors for Optoelectronic Synaptic Memristors: Deposition Techniques, Key Performance Parameters, and Applications," *ACS Applied Electronic Materials* 6, no. 1 (2024): 73–119.

8. J. d. Valle, J. G. Ramírez, M. J. Rozenberg, and I. K. Schuller, "Challenges in Materials and Devices for Resistive-Switching-Based Neuromorphic Computing," *Journal of Applied Physics* 124, no. 21 (2018): 211101.

9. I. K. Schuller, R. Stevens, R. Pino, and M. Pechan, "Neuromorphic Computing – From Materials Research to Systems Architecture Roundtable," *DOE Report* (2015).

10. F. J. Morin, "Oxides Which Show a Metal-to-Insulator Transition at the Neel Temperature," *Physical Review Letters* 3, no. 1 (1959): 34.

11. Y. Liu, A. Liu, X. Chai, et al., "An Interesting Functional Phase Change Material VO_2: Response to Multivariate Control and Extensive Applications in Optics and Electronics," *Advanced Electronic Materials* 10, no. 4 (2024): 2300699.

12. M. H. Rahman and M. A. K. Hamid, "Solid-State Oscillator Using a VO_2 Polyconductor Film as a Circuit Element," *International Journal of Electronics* 42, no. 1 (1977): 65–72.

13. B. Fisher, "Voltage Oscillations in Switching VO_2 Needles," *Journal of Applied Physics* 49, no. 9 (1978): 5339–5341.

14. M. M. Qazilbash, M. Brehm, B. G. Chae, et al., "Mott Transition in VO_2 Revealed by Infrared Spectroscopy and Nano-Imaging," *Science* 318, no. 5857 (2007): 1750–1753.

15. N. Ghazikhanian, J. del Valle, P. Salev, et al., "Resistive Switching Localization by Selective Focused Ion Beam Irradiation," *Applied Physics Letters* 123 (2023): 123505.

16. S. Cheng, M.-H. Lee, X. Li, et al., "Operando Characterization of Conductive Filaments During Resistive Switching in Mott VO_2," *Proceedings of the National Academy of Sciences USA* 118 (2021): e2013676118.

17. E. Anouchi, T. Yamin, and A. Sharoni, “Three-Terminal VO_2-Based Device with Internal Read-Write Switching,” *Physical Review Applied* 19 (2023): 034057.

18. A. Velichko, V. Putrolaynen, and M. Belyaev, “Higher-Order and Long-Range Synchronization Effects for Classification and Computing in Oscillator-Based Spiking Neural Networks,” *Neural Computing and Applications* 33 (2020): 3113–3131.

19. E. Qiu, Y.-H. Zhang, M. D. Ventra, and I. K. Schuller, “Reconfigurable Cascaded Thermal Neuristors for Neuromorphic Computing,” *Advanced Materials* 36, no. 6 (2024): 2306818.

20. G. Li, Z. Wang, Y. Chen, J.-C. Jeon, and S. S. P. Parkin, “Computational Elements Based on Coupled VO_2 Oscillators via Tunable Thermal Triggering,” *Nature Communications* 15 (2024): 5820.

21. C. V. S. Kumar, F. Maury, and N. Bahlawane, “Vanadium Oxide as a Key Constituent in Reconfigurable Metamaterials,” in *Metamaterials and Metasurfaces*, ed. J. Canet-Ferrer (IntechOpen, 2018), ch. 8.

22. N. Vardi, E. Anouchi, T. Yamin, et al., “Ramp-Reversal Memory and Phase-Boundary Scarring in Transition Metal Oxides,” *Advanced Materials* 29, no. 21 (2017): 1605029.

23. E. Anouchi, N. Vardi, Y. Kalcheim, I. K. Schuller, and A. Sharoni, “Universality and Microstrain Origin of the Ramp Reversal Memory Effect,” *Physical Review B* 106, no. 20 (2022): 205145.

24. A. Fried, O. Gotesdyner, I. Feldman, A. Kanigel, and A. Sharoni, “A New Memory Effect in Bulk Crystals of 1T-TaS_2,” *Advanced Functional Materials* (2025).

25. S. Basak, Y. Sun, M. A. Banguero, et al., “Spatially Distributed Ramp Reversal Memory in VO_2,” *Advanced Electronic Materials* 9, no. 10 (2023): 2300085.

26. A. Sharoni, J. G. Ramírez, and I. K. Schuller, “Multiple Avalanches across the Metal-Insulator Transition of Vanadium Oxide Nanoscaled Junctions,” *Physical Review Letters* 101, no. 2 (2008): 026404.

27. S. Basak, M. A. Banguero, L. Burzawa, et al., “Deep Learning Hamiltonians from Disordered Image Data in Quantum Materials,” *Physical Review B* 107 (2023): 205121.

28. S. Liu, B. Phillabaum, E. W. Carlson, et al., “Random Field Driven Spatial Complexity at the Mott Transition in VO_2,” *Physical Review Letters* 116, no. 3 (2016): 036401.

29. H.-M. You, U. M. Gösele, and T. Y. Tan, “Simulation of the Transient Indiffusion-Segregation Process of Triply Negatively Charged Ga Vacancies in GaAs and AlAs/GaAs Superlattices,” *Journal of Applied Physics* 74, no. 4 (1993): 2461–2470.

30. J. P. Sethna, K. Dahmen, S. Kartha, J. A. Krumhansl, B. W. Roberts, and J. D. Shore, “Hysteresis and Hierarchies: Dynamics of Disorder-Driven First-Order Phase Transformations,” *Physical Review Letters* 70 (1993): 3347–3350.

31. S. Wang, J. G. Ramírez, and I. K. Schuller, “Avalanches in Vanadium Sesquioxide Nanodevices,” *Physical Review B* 92, no. 8 (2015): 085150.

32. H. E. Stanley, “Scaling, Universality, and Renormalization: Three Pillars of Modern Critical Phenomena,” *Reviews of Modern Physics* 71 (1999): S358–S366.

33. J.-G. Ramírez, A. Sharoni, Y. Dubi, M. E. Gómez, and I. K. Schuller, “First-Order Reversal Curve Measurements of the Metal–Insulator Transition in VO_2: Signatures of Persistent Metallic Domains,” *Physical Review B* 79, no. 23 (2009): 235110.

34. M. Alzate Banguero, S. Basak, N. Raymond, et al., “Optical Mapping and On-Demand Selection of Local Hysteresis Properties in VO_2,” *Condensed Matter* 10, no. 1 (2025): 12.

35. P. Schofield, A. Bradicich, R. M. Gurrola, et al., “Harnessing the Metal–Insulator Transition of VO_2 in Neuromorphic Computing,” *Advanced Materials* 35, no. 37 (2023): 2205294.

36. Y. Cui, B. Liu, L. Chen, H. Luo, and Y. Gao, “Formation Energies of Intrinsic Point Defects in Monoclinic VO_2 Studied by First-Principles Calculations,” *AIP Advances* 6, no. 10 (2016): 105301.

37. K. K. Gomes, A. N. Pasupathy, A. Pushp, S. Ono, Y. Ando, and A. Yazdani, “Visualizing Pair Formation on the Atomic Scale in the High-T_c Superconductor $Bi_2Sr_2CaCu_2O_8 + \delta$,” *Nature* 447 (2007): 569–572.

38. W. O. Tromp, T. Benschop, J.-F. Ge, et al., “Puddle Formation and Persistent Gaps Across the Non-Mean-Field Breakdown of Superconductivity in Overdoped $(Pb,Bi)_2Sr_2CuO_6 + \delta$,” *Nature Materials* 22, no. 6 (2023): 703–709.

39. J. Martin, N. Akerman, G. Ulbricht, et al., “Observation of Electron–Hole Puddles in Graphene Using a Scanning Single-Electron Transistor,” *Nature Physics* 4, no. 2 (2008): 144–148.

40. I. Battisti, K. M. Bastiaans, V. Fedoseev, et al., “Universality of Pseudogap and Emergent Order in Lightly Doped Mott Insulators,” *Nature Physics* 13, no. 1 (2016): 21–25.

41. Z. Wang, Y. Okada, J. O’Neal, et al., “Disorder Induced Power-Law Gaps in an Insulator–Metal Mott Transition,” *Proceedings of the National Academy of Sciences* 115, no. 44 (2018): 11 198–11 202.

42. J. A. Bert, B. Kalisky, C. Bell, et al., “Direct Imaging of the Coexistence of Ferromagnetism and Superconductivity at the $LaAlO_3/SrTiO_3$ Interface,” *Nature Physics* 7 (2011): 767–771.

43. J. Biscaras, N. Bergeal, S. Hurand, et al., “Multiple Quantum Criticality in a Two-Dimensional Superconductor,” *Nature Materials* 12 (2013): 542–546.

44. A. Moreo, S. Yunoki, and E. Dagotto, “Phase Separation Scenario for Manganese Oxides and Related Materials,” *Science* 283, no. 5410 (1999): 2034–2040.

45. D. Cho, K. M. Bastiaans, D. Chatzopoulos, G. D. Gu, and M. P. Allan, “A Strongly Inhomogeneous Superfluid in an Iron-Based Superconductor,” *Nature* 571, no. 7766 (2019): 541–545.

46. G. McCartney, T. Hacker, and B. Yang, “Empowering faculty: A Campus Cyberinfrastructure Strategy for Research Communities,” *EDUCAUSE Review* (2014).

Supporting Information

Additional supporting information can be found online in the Supporting Information section.

Supporting Information